Editors' Suggestion | Featured in Physics

High Harmonic Generation in a Correlated Electron System

Shohei Imai, Atsushi Ono, and Sumio Ishihara
Department of Physics, Tohoku University, Sendai 980-8578, Japan

(Received 12 July 2019; revised manuscript received 20 December 2019; accepted 11 March 2020; published 16 April 2020)

High harmonic generation in crystalline solids has been examined so far on the basis of one-body energy-band structures arising from electron itineracy in a periodic potential. Here, we show the emergence of high harmonic generation signals which are attributed to the dynamics of many-body states in a low-dimensional correlated electron system. An interacting fermion model and its effective pseudospin model on a one-dimensional dimer-type lattice are analyzed. Observed high harmonic generation signals in a spontaneously symmetry-broken state, where charge densities are polarized inside of dimer units, show threshold behavior with respect to light amplitude and are interpreted in terms of tunneling and recombination of kink-antikink excitations in an electric field.

DOI: 10.1103/PhysRevLett.124.157404

Photoinduced nonequilibrium electron dynamics in solids have attracted much attention of researchers not only in condensed matter physics but also in optical physics. Recent great progress in intense laser pulse, ultrafast time-resolved experimental probes, and theoretical methods for nonequilibrium systems has opened up a new research field of exotic light-induced phenomena, for example, photo-induced superconductivity [1,2], Floquet topological phase transitions [3–5], and so on. These phenomena have been observed in wide classes of crystalline solids, owing to competition and cooperation between the wave and particle characters of electrons.

High harmonic generation (HHG) is one of the attractive phenomena induced by intense laser light [6–8]. This is a nonlinear and nonperturbative light-matter coupled phenomenon, and is widely recognized to be utilized to generate the attosecond x-ray laser pulse. Studies of HHG have been developed in atom- and molecule-gas systems [9–14], in which the HHG spectra consist of a characteristic plateau and cut-off energy. This behavior is well explained by the three-step model, i.e., a sequential process of ionization, forced oscillatory motion, and recombination of electrons in atomic and molecular potentials [12,13]. In crystalline solids, electronic processes involved in HHG are considered on the basis of the Bloch energy bands due to electron itineracy [6–8,15–29]. An extended three-step model based on the band structure was proposed to explain the characteristic plateau in HHG [24–26].

Beyond conventional semiconductors and metals, to which the one-body Bloch-band picture is applicable, correlated electron systems have great potentialities of HHG. In recent years, HHG has started to be examined in correlated electron systems from a viewpoint of the quasiparticle motion [30–35]. Large energy scales and fast dephasing due to the strong electron-electron Coulomb interactions [14,18,27,29] are of great advantage for HHG. One example is a large third harmonic generation in a perturbative regime observed in one-dimensional copper oxides [36,37]. Multiple degrees of freedom, i.e., spin, charge, orbital, and electric dipole, and their long-range orders are also unique in correlated electron materials. These characteristics are controlled not only by the electric field but also by other external fields, and supply new elementary excitations in solids, which provide large potentials for novel mechanisms and sources of HHG.

In this Letter, we show that HHG spectra emerge owing to many-electron dynamics in a correlated electron system, rather than the Bloch electron itineracy. We analyze photo-induced dynamics of an interacting fermion model on a dimer-type lattice and its low-energy effective model described by the pseudospin (PS) operators. We find emergence of HHG spectra in a spontaneously symmetry-broken state, in which charge densities are polarized inside of dimer units. The HHG spectra show a threshold behavior with respect to light amplitude. As shown in Fig. 1(c), the observed HHG are explained by an extended three-step like process for many-body kink-antikink excitations, which are valid even without electron itineracy.

A target system of the present study is an interacting electron system with a one-dimensional dimer-type lattice structure shown in Fig. 1(a). It is well known that when the average number of electrons is 0.5 per site under a strong on-site electron interaction, there are two competing electronic states in the ground state (GS): a Mott insulating state where the bonding-orbital band is half filled, termed the dimer Mott (DM) insulating state, and the polar charge-ordered (CO) state where electron distribution inside the each dimer unit breaks the inversion symmetry [see Fig. 1(c)] [38–40]. We analyze the two model Hamiltonians introduced below [41]. An interacting spinless-fermion model in a dimer lattice is defined as

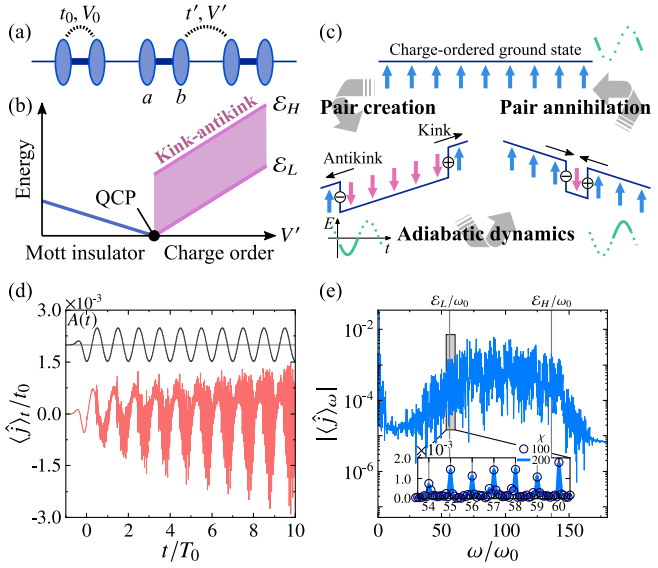

FIG. 1. (a) Schematic dimer-type lattice and interactions. The ovals and the thick bars represent atoms and dimer bonds, respectively. (b) Schematic kink-antikink excitation spectra in the TI model. A shaded area represents the kink-antikink band in the CO state. (c) Sketches of the PS configurations, the kink-antikink pair, and the present HHG process. The arrows represent the pseudospin directions; up (down) arrows correspond right (left) directed electric-dipole moments inside of the dimer unit. The steps represent the kinks and antikinks. A down pseudospin domain grows in the negative E, and shrinks and disappears in the positive E. (d) Time profiles of $A(t)$ and $\langle \hat{j} \rangle_t$. (e) Fourier transform of the current $\langle \hat{j} \rangle_\omega$. The iTEBD method is utilized in (d) and (e). The inset of (e) shows an enlargement and the results with $\chi = 100$ and 200. We set $V'/(4t_0) = 2.4$, $A_0 = 5.8$, $\omega_0/t_0 = 0.1$, and $\tau = \pi/(2\omega_0)$.

$$\mathcal{H}_{\mathrm{SF}} = -\sum_i (t_0 f_{ia}^\dagger f_{ib} + \mathrm{H.c.}) - \sum_i (t' f_{ib}^\dagger f_{i+1a} + \mathrm{H.c.}) + V_0 \sum_i n_{ia} n_{ib} + V' \sum_i n_{ib} n_{i+1a}, \quad (1)$$

where $f_{i\gamma}^\dagger$ ($f_{i\gamma}$) is the creation (annihilation) operator of a spinless fermion at the ith unit cell and sublattice $\gamma (= a, b)$, and $n_{i\gamma} = f_{i\gamma}^\dagger f_{i\gamma}$ is the number operator. The first two terms represent the fermion hoppings, and the last two terms describe the intersite Coulomb interactions. The total number of the fermions is set to N with N being the total number of the dimer units. We analyze another Hamiltonian for an interacting PS system as a low-energy effective model of $\mathcal{H}_{\mathrm{SF}}$ [39,42]. The local electronic states inside the dimer unit are described by the PS operator: the up and down PSs imply the states where electron occupies the a (left) and b (right) sites in the dimer unit, respectively. The low-energy physics is mapped onto the transverse Ising (TI) model defined by

$$\mathcal{H}_{\mathrm{TI}} = -\frac{V'}{4} \sum_{\langle ij \rangle} \sigma_i^z \sigma_j^z - t_0 \sum_i \sigma_i^x, \quad (2)$$

where $\boldsymbol{\sigma}_i$ are the Pauli matrices located at the ith unit cell. The first term ($\mathcal{H}_I$) and the second term ($\mathcal{H}_T$) describe the interaction between the nearest neighbor unit cells, and the transverse field, respectively. These terms correspond to the interdimer Coulomb interaction and the intradimer hopping in Eq. (1), respectively [43]. This model is suitable to study the collective excitations, i.e., the kink and antikink (domain-wall) excitations.

A vector potential of light is introduced as the Peierls phase as $t_0 \to t_0 e^{-iA(t)}$ and $t' \to t' e^{-iA(t)}$ in Eq. (1), where $A(t)$ is the vector potential at time t and the difference in the bond lengths are neglected. The electric field is given by $E(t) = -\partial A(t)/\partial t$. This coupling corresponds to the rotation of the transverse field as follows [41]: $\mathcal{H}_T$ is replaced by $-t_0 \sum_i [\cos A(t) \sigma_i^x - \sin A(t) \sigma_i^y]$, and the electric current operator is identified as $\hat{j}(t) = -(t_0/N) \sum_i [\sin A(t) \sigma_i^x + \cos A(t) \sigma_i^y]$. We confirmed that the numerical results of HHG in the above two models qualitatively coincide in the polar CO state, and we mainly present the results for the TI model.

The GS and excited states in the TI model without the light field have been settled [44]. The GS is the DM insulating state (a paramagnetic PS state), i.e., $\langle \sigma^z \rangle = 0$ for $V'/(4t_0) < 1$, and is the polar CO state (a ferromagnetic PS state) with spontaneous symmetry breaking of the space-inversion symmetry, i.e., $\langle \sigma^z \rangle \neq 0$ for $V'/(4t_0) > 1$. The boundary at $V'/(4t_0) = 1$ is the quantum critical point (QCP). In order to calculate the transient dynamics induced by the light field in the thermodynamic limit, the infinite time-evolving block decimation (iTEBD) method is adopted [45]. The second-order Suzuki-Trotter decomposition is utilized to calculate the time evolution of the wave function $|\psi(t + \delta t)\rangle \approx e^{-i\mathcal{H}(t)\delta t} |\psi(t)\rangle$ with a small time difference δt and the time-dependent Hamiltonian $\mathcal{H}(t)$. In most of the numerical calculations, the maximum number of the matrix dimension (χ) in the iTEBD method, and the time difference are chosen to $\chi = 200$ and $\delta t = 0.01/t_0$, respectively, which are enough to obtain well convergent results as shown later [see inset of Fig. 1(e)]. We also adopt the exact diagonalization (ED) method based on the Lanczos algorithm for finite-size clusters, where the total number of dimer units is $N = 16$ and 18 with the periodic-boundary condition. The optical absorption spectra [see Fig. S.4 in the Supplemental Material (SM)] is schematically depicted in Fig. 1(b). In the polar CO state, the excitation spectra are attributed to the kink-antikink pair excitations, and exhibit a continuous band where the upper and lower edges of the band are $\mathcal{E}_H = 4(V'/4 + t_0)$ and $\mathcal{E}_L = 4(V'/4 - t_0)$, respectively. As shown in Fig. 1(c), the electric-dipole moments inside of the dimer units align along cooperatively, represented as the all-pseudospins up state. The low-energy excitations are given from this state by flipping the pseudospins, in which the boundaries between the up- and down-pseudospin regions, i.e., $(\cdots \downarrow\downarrow\uparrow\uparrow \cdots)$ and $(\cdots \uparrow\uparrow\downarrow\downarrow \cdots)$ are termed

kink and antikink, respectively. The excitations are characterized by the number of the kink-antikink pairs, and their momenta. In the DM state, the low-energy collective excitation is located at $2(t_0 - V'/4)$.

First, we show the HHG spectra in the polar CO state $[V'/(4t_0) = 2.4]$ in the continuous-wave (cw) light. We set $A(t) = -A_0 e^{-t^2/(2\tau^2)} \cos(\omega_0 t)$ for $t < 0$, and $A(t) = -A_0 \cos(\omega_0 t)$ for $t > 0$ with frequency ω_0, amplitude A_0, and raising time τ. Numerical values of ω_0 are chosen to be much smaller than the excitation energy gap $\Delta_{\rm gap} = \mathcal{E}_L$. Time profiles of the electric current $\langle \hat{j} \rangle_t$ and its Fourier transform $\langle \hat{j} \rangle_\omega$, as well as $A(t)$, are shown in Figs. 1(d) and 1(e). A multiple pulselike profile with a period of $T_0 \equiv 2\pi/\omega_0$ appears in $\langle \hat{j} \rangle_t$, and a series of sharp spikes at $\omega = n\omega_0$ with an integer number n appears in $\langle \hat{j} \rangle_\omega$ [see inset of Fig. 1(e)]. The HHG spectra show a plateau, indicating the nonperturbative processes, approximately in the kink-antikink band. Owing to the breaking of the space-inversion symmetry in the GS, both the odd and even orders of high harmonics emerge. Overall features mentioned above do not depend on $\chi(\geq 100)$ and are almost reproduced by the ED method in finite-size clusters as shown in Fig. S.2 in SM.

The HHG spectra are sensitive to the light amplitude A_0. In Figs. 2(a) and 2(b), the intensity map of $\langle \hat{j} \rangle_\omega$ in the $\omega - A_0$ plane and its enlargement are shown, respectively. The threshold behavior of the HHG spectra with respect to A_0 is clearly seen. We find that the threshold decreases with decreasing V' (see Fig. S.1 in SM).

The observed HHG is understood by repetition of dynamics induced by a one-cycle pulse. Thus, to reveal the threshold behavior in more detail, we examine responses to a one-cycle pulse given by $A(t) = -A_0 e^{-t^2/(2\tau^2)} \cos(\omega_0 t)$. Using the iTEBD method, we analyze the absorbed energy defined by $\Delta\mathcal{E} \equiv \mathcal{E}(t \gg \tau) - \mathcal{E}(t \ll -\tau)$ with total energy $\mathcal{E} = \langle \mathcal{H}_{\rm TI} \rangle / N$, which reflects the population of the excited states. In Fig. 2(c), we plot $\Delta\mathcal{E}$ as a function of $1/E_0$ with the electric field amplitude $E_0 \equiv A_0\omega_0$. We note that, instead of the vector potential, a response to the electric field is suitable to examine the breakdown phenomena which will be introduced later. The exponential dependence is observed as $\Delta\mathcal{E} \propto \exp(-E_{\rm th}/E_0)$ with a threshold electric field $E_{\rm th}$. A deviation of data from this function for $\Delta\mathcal{E}/t_0 < 10^{-9}$ is attributed to the numerical artifact. This behavior implies a nonperturbative process in HHG, and is reproduced by the ED method [see Fig. S.3(c) in SM]. The threshold amplitude calculated in several values of V' is scaled by the excitation energy gap $\Delta_{\rm gap} = 4(V'/4 - t_0)$ as $E_{\rm th} \propto \Delta_{\rm gap}^{\alpha}$ with $\alpha \sim 1.59$ as shown in Fig. 2(d). This indicates a Landau-Zener-like breakdown in the HHG, except for the exponent which is different from $\alpha = 2$ in the case of a static field.

The HHG spectra and their characteristic time profiles are interpreted through the following analysis based on adiabatic kink-antikink dynamics. We consider the TI

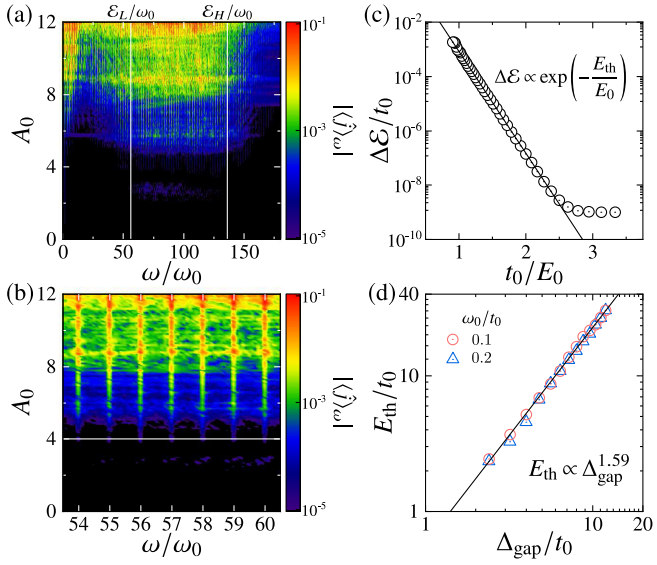

FIG. 2. (a) Intensity maps of $\langle \hat{j} \rangle_\omega$. (b) An enlargement of (a). The horizontal line indicates threshold intensity. (c) A logarithmic plot of $\Delta\mathcal{E}$ as a function of $1/E_0$. The bold line shows $\Delta\mathcal{E} \propto \exp(-E_{\rm th}/E_0)$. (d) $E_{\rm th}$ as a function of $\Delta_{\rm gap}$. The bold line shows $E_{\rm th} \propto \Delta_{\rm gap}^{\alpha}$ with $\alpha \sim 1.59$. We set $V'/(4t_0) = 2.4$, $\omega_0/t_0 = 0.1$, and $\tau = \pi/(2\omega_0)$ in (a) and (b), $\tau = 1/\omega_0$ in (c) and (d). The iTEBD method is utilized.

model in an electric field, $\mathcal{H}_{\rm TI} - [E(t)/2] \sum_i \sigma_i^z$, and examine this by using the ED method. The current operator in this case is defined in Eq. (S.8) in SM. The energy levels as functions of a static electric field $E(t) = E_s$ are shown in Fig. 3(a). The eigenwave function and eigenenergy for finite E_s are denoted by $|\phi_i(E_s)\rangle$ and $\mathcal{E}_i(E_s)$ $(i \geq 0)$, respectively, which are adiabatically connected to the ith eigenstate at $E_s = 0$. The GS at $E_s = 0$ are doubly degenerated in the thermodynamic limit, i.e., the all-up and all-down states, schematically $|\cdots\uparrow\uparrow\uparrow\uparrow\uparrow\cdots\rangle$ and $|\cdots\downarrow\downarrow\downarrow\downarrow\downarrow\cdots\rangle$, respectively, and the excited states are continuum with the finite excitation gap from GS. With increasing E_s, the energy of the all-up (all-down) state decreases (increases).

Then, we examine the current induced by the cw field shown in Figs. 1(c) and 3(c) (red line) from a viewpoint of the adiabatic dynamics of many-body states. The wave function at time t is expanded as $|\psi(t)\rangle = \sum_{i\geq 0} c_i |\phi_i(E_s)\rangle \exp[-i\mathcal{E}_i(E_s)t]$ with coefficients $c_i = \langle \phi_i(E_s)|\psi(t)\rangle$. Since $|c_0|^2 \approx 1$ and $|c_{i\geq 1}|^2 \ll 1$ as shown in Fig. 3(d), the current at time t is approximately given by $\langle \hat{j} \rangle_t = \langle \psi(t)|\hat{j}|\psi(t)\rangle \approx \sum_{i>0} c_i c_0^* \langle \phi_0(E_s)|\hat{j}|\phi_i(E_s)\rangle \exp[-i\{\mathcal{E}_i(E_s) - \mathcal{E}_0(E_s)\}t] + \text{c.c.}$ In Fig. 3(c), we compare a time profile of the current calculated by the above method shown by the blue line with that by the real-time evolution. We adopt the most dominant excited state among $|\phi_i(E_s)\rangle$'s. The two results almost coincide. We conclude that this picture based on the adiabatic dynamics is valid to understand the real-time processes in the present HHG.

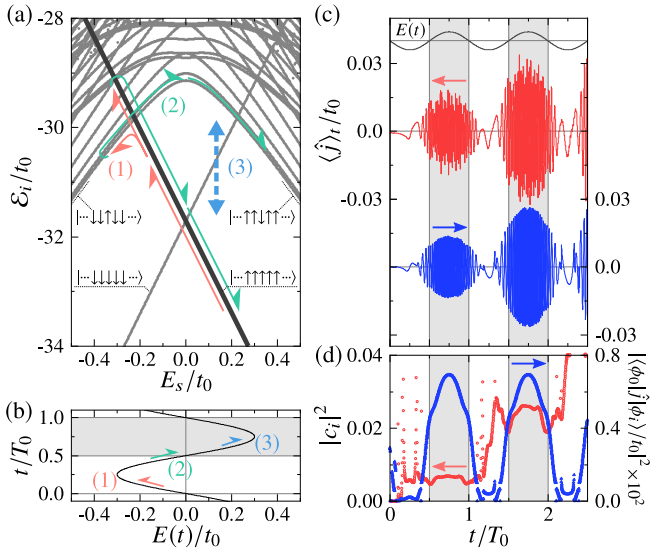

FIG. 3. Results based on the adiabatic kink-antikink dynamics. (a) Energy level diagram as a function of E_s. The bold line represents the adiabatic energy of the all-up state at $E_s = 0$. (b) A schematic time profile of $E(t)$. (c) Time profiles of $E(t)$ (black line) and $\langle\hat{j}\rangle_t$ (red line). The blue line shows the results calculated from the energy level diagram in (a) (see text). (d) Time profiles of the population of the most dominant excited state $|c_i|^2$ (red circles), and a square of the transition amplitude $|\langle\phi_0(E_s)|\hat{j}|\phi_i(E_s)\rangle|^2$ (blue triangles). Shaded areas in (b)–(d) represent time domains where $E(t)$ is positive. We set $V'/(4t_0) = 1.6$, $A_0 = 3.6$, $\omega_0/t_0 = 0.1$, $\tau = \pi/(2\omega_0)$, and $N = 18$.

The facts $|c_0|^2 \approx 1$ and $|c_{i\geq1}|^2 \ll 1$ reflect the off-resonant excitation with the light frequency $\omega_0 \ll \Delta_{\rm gap}$, and nonperturbative tunneling processes are incorporated in c_i for $i \geq 1$. In the time profile of $\langle\hat{j}\rangle_t$ in Fig. 3(c), a fine oscillation is attributed to the factor $\exp[-i\{\mathcal{E}_i(E_s) - \mathcal{E}_0(E_s)\}t]$. An envelope with a period of T_0, showing large amplitude in regions with positive $E(t)$ [shaded areas in Fig. 3(c)], is due to the amplitude factor $c_i\langle\phi_0(E_s)|\hat{j}|\phi_i(E_s)\rangle$. As shown in Fig. 3(d), this characteristic time profile of the amplitude factor does not originate mainly from populations of the excited state $|c_i|^2$, but the transition amplitude $|\langle\phi_0(E_s)|\hat{j}|\phi_i(E_s)\rangle|$. This means that the many-body character of the wave function governs the transition amplitude in the present case as discussed below.

Now, a microscopic process of the HHG is explained by the adiabatic many-body energy diagram in Fig. 3(a). Let us start from the all-up state, $|\cdots\uparrow\uparrow\uparrow\uparrow\uparrow\cdots\rangle$, at $E_s = 0$ as a symmetry-broken GS. The first excited state at $E_s = 0$ is given by a liner combination of the single kink-antikink excitation states, and is adiabatically connected to $|\cdots\downarrow\downarrow\uparrow\downarrow\downarrow\cdots\rangle$ in the limit of $E_s \to -\infty$. With decreasing E_s from zero, the energy level of the all-up state increases and anticrosses with the excited state [(1) in Figs. 3(a) and (b)]. This anticrossing point is known as the quantum spinodal point [46,47]. Through the Landau-Zener transition, the adiabatic GS state transfers with finite probability to the excited state $|\cdots\downarrow\downarrow\uparrow\downarrow\downarrow\cdots\rangle$ at a certain negative E_s. However, the transition amplitude $\langle\phi_0(E_s)|\hat{j}|\phi_i(E_s)\rangle$ is almost zero between the all-up state and this excited state, since the current operator proportional to $\sum_i \sigma_i^y$ brings about one PS flip. When a sign of $E(t)$ is turned into positive, the excited state moves adiabatically [(2) in Figs. 3(a) and 3(b)], and is changed into $|\cdots\uparrow\uparrow\downarrow\uparrow\uparrow\cdots\rangle$ at large positive E_s. The transition amplitude $\langle\phi_0(E_s)|\hat{j}|\phi_i(E_s)\rangle$ becomes finite, and the induced current emits light [(3) in Figs. 3(a) and 3(b)]. This description based on the many-body states corresponds to the three-step model known for the atoms and semiconductors, and is valid at least in the region where A_0 is close to the threshold and $V'/(4t_0) \gtrsim 2.4$.

So far, effects of the electron itinerancy are neglected in the above calculations. In Figs. 4(a) and 4(b), we show $\langle\hat{j}\rangle_t$ and $\langle\hat{j}\rangle_\omega$ in the interacting fermion model given in Eq. (1), where the polar CO state is realized for $V' \gg t_0, t'$. The contribution from the interdimer current is less than 10% even though $t' = 0.5t_0$ [see green line in Fig. 4(a)]. We conclude that the essential characters in the HHG in the polar CO state is not governed by the electron propagation over the dimer units, but by the kink-antikink excitations and propagations.

Experimental observations are crucial to confirm the present theoretical prediction for a new mechanism of HHG. Candidate materials are low-dimensional organic molecular solids, $(TMTTF)_2X$ (TMTTF = tetramethyltetrathiafulvalene, $X = PF_6$, AsF_6), which show the polar CO phase in low temperatures and have an energy gap of several tens of terahertz [48–51]. Parameter values for the light field are $\omega_0 \sim$ a few terahertz and $E_0 \sim 10$ MV/cm, which can be realized in recent progress of the laser technology. The present proposal will be verified by experiments; the HHG spectra do not appear in the electron-hole excitation bands but in the many-body

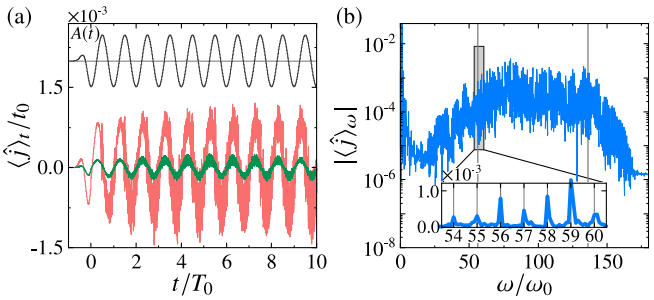

FIG. 4. Results in the spinless-fermion model in the cw field. (a) Time profiles of $A(t)$ (upper) and $\langle\hat{j}\rangle_t$ [red (light gray) line in lower]. The green (dark gray) line in lower represents the interdimer current. (b) Fourier transform of the current, $\langle\hat{j}\rangle_\omega$. The inset shows an enlargement. We set $V'/(4t_0) = 2.4$, $V_0/V' = 1$, $t'/t_0 = 0.5$, $A_0 = 5.8$, $\omega_0/t_0 = 0.1$, and $\tau = \pi/(2\omega_0)$. The iTEBD method is utilized.

excitation band, which can be checked by comparing the HHG and linear optical absorption spectra, and are reduced by collapsing the long-range dipole order with increasing temperature and external fields.

The authors would like to thank Y. Masaki, S. Iwai, and M. Naka for their fruitful discussions. This work was supported by JSPS KAKENHI, Grants No. JP17H02916, No. JP18H05208, and No. JP19K23419. Some of the numerical calculations were performed using the facilities of the Supercomputer Center, the Institute for Solid State Physics, The University of Tokyo.

[1] D. Fausti, R. I. Tobey, N. Dean, S. Kaiser, A. Dienst, M. C. Hoffmann, S. Pyon, T. Takayama, H. Takagi, and A. Cavalleri, Science **331**, 189 (2011).
[2] M. Mitrano, A. Cantaluppi, D. Nicoletti, S. Kaiser, A. Perucchi, S. Lupi, P. Di Pietro, D. Pontiroli, M. Riccò, S. R. Clark, D. Jaksch, and A. Cavalleri, Nature (London) **530**, 461 (2016).
[3] R. Moessner and S. L. Sondhi, Nat. Phys. **13**, 424 (2017).
[4] N. Goldman, J. C. Budich, and P. Zoller, Nat. Phys. **12**, 639 (2016).
[5] T. Oka and S. Kitamura, Annu. Rev. Condens. Matter Phys. **10**, 387 (2019).
[6] U. Huttner, M. Kira, and S. W. Koch, Laser Photonics Rev. **11**, 1700049 (2017).
[7] S. Y. Kruchinin, F. Krausz, and V. S. Yakovlev, Rev. Mod. Phys. **90**, 021002 (2018).
[8] S. Ghimire and D. A. Reis, Nat. Phys. **15**, 10 (2019).
[9] P. Agostini and L. F. DiMauro, Rep. Prog. Phys. **67**, 813 (2004).
[10] F. Krausz and M. Ivanov, Rev. Mod. Phys. **81**, 163 (2009).
[11] L. Gallmann, C. Cirelli, and U. Keller, Annu. Rev. Phys. Chem. **63**, 447 (2012).
[12] P. B. Corkum, Phys. Rev. Lett. **71**, 1994 (1993).
[13] M. Lewenstein, P. Balcou, M. Y. Ivanov, A. L'Huillier, and P. B. Corkum, Phys. Rev. A **49**, 2117 (1994).
[14] K. L. Ishikawa and T. Sato, IEEE J. Sel. Top. Quantum Electron. **21**, 8700916 (2015).
[15] S. Ghimire, A. D. DiChiara, E. Sistrunk, P. Agostini, L. F. DiMauro, and D. A. Ries, Nat. Phys. **7**, 138 (2011).
[16] M. Hohenleutner, F. Langer, O. Schubert, M. Knorr, U. Huttner, S. W. Koch, M. Kira, and R. Huber, Nature (London) **523**, 572 (2015).
[17] G. Ndabashimiye, S. Ghimire, M. Wu, D. A. Browne, K. J. Schafer, M. B. Gaarde, and D. A. Reis, Nature (London) **534**, 520 (2016).
[18] H. Liu, Y. Li, Y. S. You, S. Ghimire, T. F. Heinz, and D. A. Reis, Nat. Phys. **13**, 262 (2017).
[19] N. Yoshikawa, T. Tamaya, and K. Tanaka, Science **356**, 736 (2017).
[20] T. Higuchi, M. I. Stockman, and P. Hommelhoff, Phys. Rev. Lett. **113**, 213901 (2014).
[21] P. G. Hawkins, M. Y. Ivanov, and V. S. Yakovlev, Phys. Rev. A **91**, 013405 (2015).
[22] G. Vampa, C. R. McDonald, G. Orlando, P. B. Corkum, and T. Brabec, Phys. Rev. B **91**, 064302 (2015).
[23] C. R. McDonald, G. Vampa, P. B. Corkum, and T. Brabec, Phys. Rev. A **92**, 033845 (2015).
[24] M. Wu, D. A. Browne, K. J. Schafer, and M. B. Gaarde, Phys. Rev. A **94**, 063403 (2016).
[25] T. Ikemachi, Y. Shinohara, T. Sato, J. Yumoto, M. Kuwata-Gonokami, and K. L. Ishikawa, Phys. Rev. A **95**, 043416 (2017).
[26] K. K. Hansen, T. Deffge, and D. Bauer, Phys. Rev. A **96**, 053418 (2017).
[27] T. Ikemachi, Y. Shinohara, T. Sato, J. Yumoto, M. Kuwata-Gonokami, and K. L. Ishikawa, Phys. Rev. A **98**, 023415 (2018).
[28] T. N. Ikeda, K. Chinzei, and H. Tsunetsugu, Phys. Rev. A **98**, 063426 (2018).
[29] S. Y. Kruchinin, Phys. Rev. A **100**, 043839 (2019).
[30] R. E. F. Silva, I. V. Blinov, A. N. Rubtsov, O. Smirnova, and M. Ivanov, Nat. Photonics **12**, 266 (2018).
[31] Y. Murakami, M. Eckstein, and P. Werner, Phys. Rev. Lett. **121**, 057405 (2018).
[32] N. Tancogne-Dejean, M. A. Sentef, and A. Rubio, Phys. Rev. Lett. **121**, 097402 (2018).
[33] S. Takayoshi, Y. Murakami, and P. Werner, Phys. Rev. B **99**, 184303 (2019).
[34] W. Zhu, A. Chacon, and J. Zhu, arXiv:1811.12334.
[35] T. Nag, R.-J. Slager, T. Higuchi, and T. Oka, Phys. Rev. B **100**, 134301 (2019).
[36] H. Kishida, H. Matsuzaki, H. Okamoto, T. Manabe, M. Yamashita, Y. Taguchi, and Y. Tokura, Nature (London) **405**, 929 (2000).
[37] T. Ogasawara, M. Ashida, N. Motoyama, H. Eisaki, S. Uchida, Y. Tokura, H. Ghosh, A. Shukla, S. Mazumdar, and M. Kuwata-Gonokami, Phys. Rev. Lett. **85**, 2204 (2000).
[38] H. Kino and H. Fukuyama, J. Phys. Soc. Jpn. **65**, 2158 (1996).
[39] M. Naka and S. Ishihara, J. Phys. Soc. Jpn. **79**, 063707 (2010).
[40] C. Hotta, Phys. Rev. B **82**, 241104(R) (2010).
[41] See Supplemental Material at http://link.aps.org/supplemental/10.1103/PhysRevLett.124.157404 for more details on derivation of the effective models and introduction of the light field in the models.
[42] M. Tsuchiizu (private communication).
[43] All energy parameter values are fixed during each numerical calculation for the time evolution. Although a modification of the Coulomb interaction by light irradiation is proposed in Ref. [32], this is beyond the aim of the present work.
[44] P. Pfeuty, Ann. Phys. (N.Y.) **57**, 79 (1970).
[45] G. Vidal, Phys. Rev. Lett. **98**, 070201 (2007).
[46] H. De Raedt, S. Miyashita, K. Saito, D. García-Pablos, and N. García, Phys. Rev. B **56**, 11761 (1997).
[47] S. Miyashita, K. Saito, and H. De Raedt, Phys. Rev. Lett. **80**, 1525 (1998).
[48] H. H. S. Javadi, R. Laversanne, and A. J. Epstein, Phys. Rev. B **37**, 4280 (1988).
[49] V. Vescoli, F. Zwick, W. Henderson, L. Degiorgi, M. Grioni, G. Gruner, and L. K. Montgomery, Eur. Phys. J. B **16**, 487 (2000).
[50] P. Monceau, F. Ya. Nad, and S. Brazovskii, Phys. Rev. Lett. **86**, 4080 (2001).
[51] Y. Naitoh, Y. Kawakami, T. Ishikawa, Y. Sagae, H. Itoh, K. Yamamoto, T. Sasaki, M. Dressel, S. Ishihara, Y. Tanaka, K. Yonemitsu, and S. Iwai, Phys. Rev. B **93**, 165126 (2016).